Spectral and temporal properties of type-II parametric down-conversion: The impact of losses during state generation

Denis A. Kopylov [1,2,*] Michael Stefszky [2,3] Torsten Meier [1,2] Christine Silberhorn [2,3] and Polina R. Sharapova [1]

[1]*Department of Physics, Paderborn University, Warburger Str. 100, D-33098 Paderborn, Germany*

[2]*Institute for Photonic Quantum Systems (PhoQS), Paderborn University, Warburger Str. 100, D-33098 Paderborn, Germany*

[3]*Integrated Quantum Optics, Paderborn University, Warburger Str. 100, D-33098 Paderborn, Germany*

(Received 28 January 2025; accepted 18 June 2025; published 5 August 2025)

In this paper, we theoretically study the spectral and temporal properties of pulsed spontaneous parametric down-conversion (SPDC) generated in lossy waveguides. Our theoretical approach is based on the formalism of Gaussian states and the Langevin equation, which is elaborated for weak parametric down-conversion and photon-number-unresolved click detection. Using the example of frequency-degenerate type-II SPDC generated under the pump-idler group-velocity-matching condition, we show how the joint-spectral intensity, mode structure, normalized second-order correlation function, and Hong-Ou-Mandel interference pattern depend on internal losses of the SPDC process. We found that the joint-spectral intensity is almost insensitive to internal losses, while the second-order correlation function shows a strong dependence on them, being different for the signal and idler beams in the presence of internal losses. Based on the sensitivity of the normalized second-order correlation function, we show how its measurement can be used to experimentally determine internal losses.

DOI: 10.1103/zp72-7qwl

I. INTRODUCTION

Currently, for applications in quantum technologies, there is a huge demand for compact integrated sources of nonclassical light [1]. One of the flexible frameworks, which allows the experimental realization of various types of nonclassical field sources, is based on spontaneous parametric down-conversion (SPDC). The generation of photon pairs via SPDC requires a second-order nonlinear susceptibility; therefore, miniaturized integrated waveguide-based SPDC sources rely on the technologies for waveguide fabrication of such materials as KTP [2], $LiNbO_3$ [3], or GaAs [4].

Nonlinear waveguides have significant benefits compared to nonlinear bulk crystals. The guided modes provide a high degree of localization of the electromagnetic field [5], effective coupling between the pump, signal, and idler fields, and the tunability of their dispersion by the geometry of the waveguide [6]. However, imperfections during waveguide fabrication result in differences between the desired ideal and the fabricated waveguide [7], which may lead to a change of the properties of the generated states. Importantly for quantum technological applications is the determination and characterization of internal waveguide losses during SPDC. For example, signal and idler photons can be scattered due to the roughness of the waveguide surface [8]. In turn, AlGaAs waveguides, which are also used for SPDC [9,10], have a strong material absorption in their cores. Therefore, the proper description of such nonideal lossy SPDC sources is a relevant task.

SPDC sources may be characterized using one or more of several experimental techniques. Measurements of the joint spectral intensity, the normalized second-order correlation function, and the Hong-Ou-Mandel interference [11] represent standard tools [12–17]. They are convenient for bulk crystals and are also widely used for the experimental characterization of lossy waveguide sources. However, the standard description and interpretation of experimental results do not take into account the presence of internal losses.

In this paper, we highlight the fundamental difference between the pulsed SPDC generated in media with and without internal losses and explore the possibility of extracting internal losses from measurements of the second-order correlation function.

The structure of this paper is the following: In Sec. II A, we present our theoretical approach, which is based on the framework of Gaussian states and the Langevin equation. The generated PDC state is described in terms of the second-order correlation matrices, and in Sec. II B, we present explicit expressions for the joint spectral intensity and the temporal profiles of the signal and idler fields. In Sec. II C, we present the Mercer-Wolf-basis and the number of occupied modes for type-II SPDC. Sections II D and II E show how the HOM interference pattern and the normalized second-order correlation functions can be computed for Gaussian states. In Sec. II F, we summarize the advantages of our method. Section III presents and discusses the results of numerical simulations of frequency-degenerate type-II SPDC generated under the pump-idler group-velocity-matching condition. The

*Contact author: denis.kopylov@uni-paderborn.de

obtained results allow us to propose a new approach for the experimental determination of internal loss coefficients from the measured normalized second-order correlation functions, as presented in Sec. III C.

II. THEORETICAL APPROACH

A. Master equation for type-II parametric down-conversion

For the numerical analysis of parametric down-conversion (PDC) with internal losses, we use the numerical scheme that was developed in Ref. [18]. The approach is based on the framework of multimode Gaussian states [19] in a discrete uniform frequency space $(\omega_0, \omega_1, \ldots, \omega_N)$, which allows us to write the equations of motion directly in the form which are used in our numerical calculations. For type-II PDC, the nonlinear interaction produces two orthogonally polarized fields: horizontal (here TE) and vertical (TM) polarized field components. Further in the text, we call these field components signal and idler, respectively. Signal and idler fields at position z are given by two vectors of monochromatic operators: $\hat{\mathbf{a}}(z) = (\hat{a}_0(z), \hat{a}_1(z), \ldots, \hat{a}_N(z))^T$ and $\hat{\mathbf{b}}(z) = (\hat{b}_0(z), \hat{b}_1(z), \ldots, \hat{b}_N(z))^T$, respectively, where $\hat{a}_n(z) \equiv \hat{a}(z, \omega_n)$ and $\hat{b}_n(z) \equiv \hat{b}(z, \omega_n)$. These operators obey bosonic commutation relations $[\hat{a}_i(z), \hat{a}_j^\dagger(z)] = [\hat{b}_i(z), \hat{b}_j^\dagger(z)] = \delta_{ij}$ and $[\hat{a}_i(z), \hat{b}_j^\dagger(z)] = 0$. In terms of fast oscillating operators, the electric field operator for the signal field has the form

$$\hat{E}_a^+(z,t) = \sum_m \xi_a(\omega_m)\hat{a}_m(z)e^{-i\omega_m t}, \tag{1}$$

where the amplitude $\xi_a(\omega_m) = \sqrt{\frac{\hbar\omega_m}{2\varepsilon_0 c T n^a(\omega_m)}}$, $T = \frac{2\pi}{\omega_{m+1}-\omega_m}$, and $n^a(\omega_m)$ is the refractive index for the signal field. For the idler field, the index "a" should be replaced by "b."

The generator of the spatial evolution [20,21] for type-II PDC is given by $\hat{G}(z) = \hat{G}_l(z) + \hat{G}_{\text{pdc}}(z)$, where the linear part is given by

$$\hat{G}_l(z) = \sum_n \hbar k_n^a \hat{a}_n^\dagger(z)\hat{a}_n(z) + \sum_n \hbar k_n^b \hat{b}_n^\dagger(z)\hat{b}_n(z) + \text{H.c.} \tag{2}$$

and the nonlinear interaction part is

$$\hat{G}_{\text{pdc}}(z) = \frac{\hbar\Gamma}{2}\sum_{i,j} J_{ij}(z)\hat{a}_i^\dagger(z)\hat{b}_j^\dagger(z) + \text{H.c.} \tag{3}$$

Here we have assumed the pump wave to be classical, determining the coupling matrix in the form $J_{ij}(z) = S(\omega_i + \omega_j)e^{i(k^p(\omega_i+\omega_j)-k_{\text{QPM}})z}$, where $S(\omega)$ is the pump spectrum at $z = 0$. The wavevectors $k_n^{(a,b,p)} \equiv k^{(a,b,p)}(\omega_n) = \frac{n^{(a,b,p)}(\omega_n)\omega_n}{c}$ of the (a) signal, (b) idler, and (p) pump fields are determined by the corresponding dispersion profiles of a waveguide $n^{(a,b,p)}(\omega_n)$. The quasi-phase-matching condition is taken into account by $k_{\text{QPM}} = 2\pi/\Lambda$, where Λ is the poling period. The parameter Γ is proportional to the effective second-order susceptibility, the pump electric field amplitude, and the spatial overlap between the interacting fields.

As we are interested in internal PDC losses, i.e., losses during the PDC generation, we need to describe the dynamics in terms of an open quantum system [22]. For simplicity,

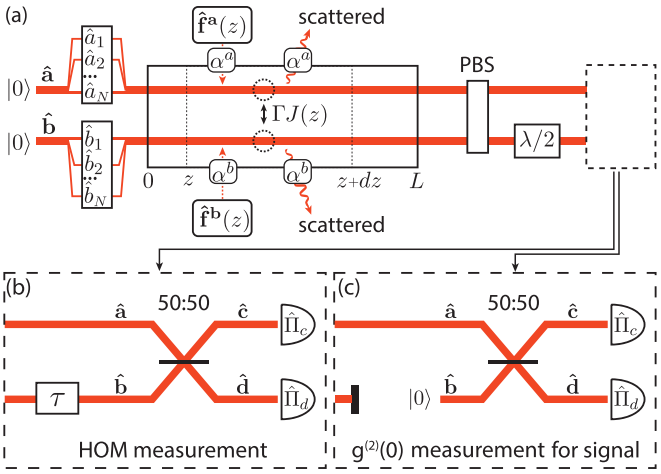

FIG. 1. (a) The PDC generation scheme in lossy media; (b) the Hong-Ou-Mandel interference scheme; and (c) scheme for measuring the normalized second-order correlation function for the signal field $g_s^{(2)}$.

we introduce two separate, noninteracting, spatially delta-correlated Markovian environments for the signal and idler modes, which allow us to introduce two sets of Langevin noise operators $\hat{f}_n^a(z) \equiv \hat{f}^a(z, \omega_n)$ and $\hat{f}_n^b(z) \equiv \hat{f}^b(z, \omega_n)$ and two frequency-dependent loss-coefficients $\alpha_n^a \equiv \alpha^a(\omega_n)$ and $\alpha_n^b \equiv \alpha^b(\omega_n)$ [see Fig. 1(a)]. The spatial Langevin equation for the operators $\hat{a}$ has the form [18]

$$\frac{d\hat{a}_n(z)}{dz} = i\kappa_n^a\hat{a}_n(z) + i\Gamma\sum_m J_{nm}(z)\hat{b}_m^\dagger(z) + \sqrt{\alpha_n^a}\hat{f}_n^a(z), \tag{4}$$

where $\kappa_n^a = k_n^a + i\alpha_n^a/2$. The Langevin equation for operators $\hat{b}$ is similar. In turn, the pump losses can easily be included in the model by changing the coupling matrix $J_{nm}(z)$. Indeed, as long as the pump field is classical, we can consider the classical solution for wave propagation in an absorbing medium. In this case, replacing the real wavevector $k^p(\omega)$ with the complex one $\kappa^p(\omega) = k^p(\omega) + i\alpha^p(\omega)/2$ will give us a decaying profile of the pump field. In the absence of all losses, the Langevin equation corresponds to the spatial Heisenberg equation [21].

In contrast to the lossless PDC case, where the solution to the Heisenberg equation has the form of a Bogoliubov transformation [23,24], the solution to the multimode Langevin equation [Eq. (4)] does not have such a simple form. However, in this paper, we consider the case where the initial state and environment are given by vacuum states, which leads to the generation of an undisplaced Gaussian state via the PDC process. Therefore, the spatial evolution of PDC light is described by a master equation for the second-order correlation functions [18]. In a discrete frequency space, the master equation constitutes a system of differential equations. To write this system in a compact matrix form, we introduce the second-order correlation matrices $\mathcal{D}(z)$ and $\mathcal{C}(z)$ as

$$\mathcal{D}(z) = \begin{pmatrix} \langle\hat{\mathbf{a}}^\dagger\hat{\mathbf{a}}\rangle_z & \langle\hat{\mathbf{a}}^\dagger\hat{\mathbf{b}}\rangle_z \\ \langle\hat{\mathbf{b}}^\dagger\hat{\mathbf{a}}\rangle_z & \langle\hat{\mathbf{b}}^\dagger\hat{\mathbf{b}}\rangle_z \end{pmatrix}, \quad \mathcal{C}(z) = \begin{pmatrix} \langle\hat{\mathbf{a}}\hat{\mathbf{a}}\rangle_z & \langle\hat{\mathbf{a}}\hat{\mathbf{b}}\rangle_z \\ \langle\hat{\mathbf{b}}\hat{\mathbf{a}}\rangle_z & \langle\hat{\mathbf{b}}\hat{\mathbf{b}}\rangle_z \end{pmatrix}. \tag{5}$$

The expressions in the form $\langle \hat{\mathbf{a}}^\dagger \hat{\mathbf{b}} \rangle_z$ and $\langle \hat{\mathbf{a}} \hat{\mathbf{b}} \rangle_z$ denote the $N \times N$ matrices with matrix elements $\langle \hat{a}_i^\dagger(z) \hat{b}_j(z) \rangle$ and $\langle \hat{a}_i(z) \hat{b}_j(z) \rangle$, respectively. The resulting master equation in a matrix form reads [18]

$$\frac{d\mathcal{D}(z)}{dz} = i(\mathcal{D}(z)K - K^*\mathcal{D}(z)) + i\Gamma(\mathcal{C}^*(z)M^T(z) - M^*(z)\mathcal{C}(z)), \tag{6}$$

$$\frac{d\mathcal{C}(z)}{dz} = i(\mathcal{C}(z)K + K\mathcal{C}(z)) + i\Gamma((M(z)\mathcal{D}(z) + M(z))^T + M(z)\mathcal{D}(z)), \tag{7}$$

where the superscript $[\cdot]^*$ denotes the complex conjugation of a matrix. The matrix K is a diagonal matrix with elements $\mathrm{diag}(\kappa_0^a, \ldots \kappa_N^a, \kappa_0^b, \ldots, \kappa_N^b)$, while the z-dependent coupling matrix $M(z)$ is given by

$$M(z) = \begin{pmatrix} \mathbf{0}_N & J(z) \\ J^T(z) & \mathbf{0}_N \end{pmatrix}. \tag{8}$$

The initial condition (vacuum state $|0\rangle$) reads $\mathcal{D}(0) = \mathcal{C}(0) = \mathbf{0}_{2N}$ and, together with the coupling matrix in the form of Eq. (8), determines the structure of the solution: i.e., for any z, the following equalities are fulfilled $\langle \hat{\mathbf{a}}^\dagger \hat{\mathbf{b}} \rangle_z = \langle \hat{\mathbf{b}}^\dagger \hat{\mathbf{a}} \rangle_z = \langle \hat{\mathbf{a}} \hat{\mathbf{a}} \rangle_z = \langle \hat{\mathbf{b}} \hat{\mathbf{b}} \rangle_z = \mathbf{0}_N$. Therefore, the correlation matrices for type-II PDC have the form

$$\mathcal{D}(z) = \begin{pmatrix} \langle \hat{\mathbf{a}}^\dagger \hat{\mathbf{a}} \rangle_z & \mathbf{0}_N \\ \mathbf{0}_N & \langle \hat{\mathbf{b}}^\dagger \hat{\mathbf{b}} \rangle_z \end{pmatrix}, \quad \mathcal{C}(z) = \begin{pmatrix} \mathbf{0}_N & \langle \hat{\mathbf{a}} \hat{\mathbf{b}} \rangle_z \\ \langle \hat{\mathbf{b}} \hat{\mathbf{a}} \rangle_z & \mathbf{0}_N \end{pmatrix}. \tag{9}$$

By solving the master equations [Eqs. (6) and (7)] from $z = 0$ till $z = L$, where L is the length of the nonlinear waveguide, the output second-order correlation matrices $\mathcal{D}(L)$ and $\mathcal{C}(L)$ are evaluated. These matrices contain all information about the quantum state.

In the next section, we show how these matrices can be used to compute spectral and temporal profiles of the signal and idler fields, the joint spectral intensity, and the effective number of occupied modes. In Secs. II D and II E the correlation matrices are used to calculate the Hong-Ou-Mandel interference and the normalized second-order correlation functions.

B. Spectral and temporal properties of PDC

The spectral photon-number distribution for the signal field is obtained from the diagonal elements of the matrix $\langle \hat{\mathbf{a}}^\dagger \hat{\mathbf{a}} \rangle_L$ as

$$\langle \hat{n}_a(\omega_m) \rangle \equiv \langle \hat{a}_m^\dagger(L) \hat{a}_m(L) \rangle \tag{10}$$

and defines the total number of photons in the signal subsystem $N_a = \sum_m \langle \hat{n}_a(\omega_m) \rangle$. In addition to the spectral distribution, the temporal profile of the signal field at $z = L$ can be found as

$$I_a(t) = \langle \hat{E}_a^-(L,t) \hat{E}_a^+(L,t) \rangle = \sum_{nm} \xi_a(\omega_n) \xi_b(\omega_m) \langle \hat{a}_n^\dagger(L) \hat{a}_m(L) \rangle \, e^{i(\omega_n - \omega_m)t}. \tag{11}$$

For the idler field, the spectral and temporal intensity profile can be found similarly by changing a to b.

It is a little more difficult to express the fourth-order moments in terms of the second-order matrices. In particular, one can define the joint spectral intensity (JSI) as

$$\mathrm{JSI}(\omega_n, \omega_m) = \langle \hat{n}_a(\omega_n) \hat{n}_b(\omega_m) \rangle \, . \tag{12}$$

In order to express the $\mathrm{JSI}(\omega_n, \omega_m)$ in terms of second-order correlations, the result derived in Ref. [25] is used and reads

$$\mathrm{JSI}(\omega_n, \omega_m) = \langle \hat{a}_n^\dagger \hat{b}_m^\dagger \rangle \langle \hat{a}_n \hat{b}_m \rangle + \langle \hat{a}_n^\dagger \hat{a}_n \rangle \langle \hat{b}_m^\dagger \hat{b}_m \rangle + \langle \hat{a}_n^\dagger \hat{b}_m \rangle \langle \hat{b}_m^\dagger \hat{a}_n \rangle \, . \tag{13}$$

C. Mode structure of PDC

In order to study the mode structure of the resulting fields, we use the broadband Mercer-Wolf modes [26,27]. These modes are nothing more than a diagonalization of the matrix $\mathcal{D}$ with the use of a unitary matrix V [18]. As long as the matrix $\mathcal{D}$ has a block-diagonal form [see Eq. (9)], $V = V_a \oplus V_b$ holds, where V_a and V_b are also unitary matrices. Therefore, for type-II PDC, the Mercer-Wolf expansion diagonalizes the signal and idler subsystems independently, allowing us to introduce broadband modes for the signal and idler subsystems separately, namely, $\hat{\mathbf{A}} = V_a^T \hat{\mathbf{a}}$ and $\hat{\mathbf{B}} = V_b^T \hat{\mathbf{b}}$, respectively. As a result, the correlation matrix $\mathcal{D}^{\mathrm{MW}}$ in the broadband Mercer-Wolf mode basis has the form

$$\mathcal{D}^{\mathrm{MW}} = V^\dagger \mathcal{D} V = \begin{pmatrix} \langle \hat{\mathbf{A}}^\dagger \hat{\mathbf{A}} \rangle & \mathbf{0}_N \\ \mathbf{0}_N & \langle \hat{\mathbf{B}}^\dagger \hat{\mathbf{B}} \rangle \end{pmatrix}, \tag{14}$$

where both the matrices $\langle \hat{\mathbf{A}}^\dagger \hat{\mathbf{A}} \rangle$ and $\langle \hat{\mathbf{B}}^\dagger \hat{\mathbf{B}} \rangle$ are diagonal.

For an arbitrary correlation matrix $\mathcal{D}$, the number of occupied modes is defined as [28]

$$\mu(\mathcal{D}) = \left(\sum_i [n_i(\mathcal{D})]^2 \right)^{-1}, \tag{15}$$

where $n_i(D) = \mathcal{D}_{ii} / (\sum_i \mathcal{D}_{ii})$.

The total effective number of Mercer-Wolf PDC modes for the joint signal-idler system is given by

$$\mu_{ab} \equiv \mu(\mathcal{D}^{\mathrm{MW}}). \tag{16}$$

Note that the matrix $\mathcal{D}^{\mathrm{MW}}$ being diagonal implies that the above expression gives the minimal number of occupied modes compared to any other broadband basis [18]. The number μ_{ab} is the total effective number of modes and, therefore, is different to the Schmidt number (the effective number of spectral modes), which is commonly defined via the Schmidt decomposition of the two-photon amplitude [29,30].

In addition, asthe Mercer-Wolf expansion diagonalizes the signal and idler subsystems independently, an effective number of occupied Mercer-Wolf modes can be defined separately for the signal and idler subsystems as

$$\mu_a \equiv \mu(\langle \hat{\mathbf{A}}^\dagger \hat{\mathbf{A}} \rangle) \quad \text{and} \quad \mu_b \equiv \mu(\langle \hat{\mathbf{B}}^\dagger \hat{\mathbf{B}} \rangle), \tag{17}$$

respectively.

Note that the Mercer-Wolf expansion for lossless type-II PDC gives the equal number of modes for the signal and idler subsystems $\mu_a = \mu_b$ and $\mu_{ab} = \mu_a + \mu_b$. In the presence of losses, the number of modes in the signal and idler subsystems can differ ($\mu_a \neq \mu_b$). In this case, the function $\mu(\cdot)$ is not additive, i.e., $\mu_{ab} \neq \mu_a + \mu_b$. Therefore, to fully characterize

a lossy PDC system, all three numbers of modes, μ_{ab}, μ_a, and μ_b, are required.

The Mercer-Wolf basis provides the matrices $\langle\hat{\mathbf{A}}^\dagger\hat{\mathbf{A}}\rangle$ and $\langle\hat{\mathbf{B}}^\dagger\hat{\mathbf{B}}\rangle$ in diagonal form. However, the correlation matrix $\langle\hat{\mathbf{A}}\hat{\mathbf{B}}\rangle = V_a^T\,\langle\hat{\mathbf{a}}\hat{\mathbf{b}}\rangle\,V_b$ is not necessarily diagonal: it can contain non-diagonal terms, indicating the presence of field correlations between Mercer-Wolf modes with different indexes.

D. The Hong-Ou-Mandel interferometer

HOM interference is typically considered under two approximations: First, the low-gain regime of PDC generation is used, where all the photon number components beyond two are neglected. The second approximation is the lossless PDC assumption, which leads to pure state generation. Under these approximation, the PDC is characterized by the two-photon amplitude (TPA), which determines the coincidence probability in the HOM experiment [31,32]. However, for the pulsed low-gain PDC with losses, the correct description of the quantum state in terms of the TPA is quite complicated. The existing approaches are developed either for PDC with a monochromatic pump [33–35], which can not describe pulsed PDC, or with the use of scattering theory [36–38], whose application is challenging for single-pass PDC generated in long waveguides.

In this section, we show how the framework of Gaussian states can be applied for the study of the HOM interference for the lossy PDC. Our approach allows us to go beyond the aforementioned approximations, and provides an accurate description of experimental scenarios. We consider two steps: (1) a linear transformation of the PDC field and (2) a detection via photon-click (on-off) detectors.

a. Linear transformation for HOM. The scheme of the HOM interferometer is shown in Figs. 1(a) and 1(b). At the output of the waveguide, the signal and idler fields have orthogonal polarizations [Fig. 1(a)]. Thus, a polarizing beamsplitter is used for the spatial separation of the signal and idler beams. To let the fields interfere at a beamsplitter, a half-wave-plate in the idler channel is used to match the polarizations of the signal and idler fields. Note that these two optical elements keep the matrices $\mathcal{D}$ and $\mathcal{C}$ unchanged.

Varying the distinguishability in HOM interference is usually achieved by adjusting the time delay between the signal and idler fields interfering on a 50:50 beamsplitter [Fig. 1(b)]. Both these elements are described by unitary transformations of annihilation operators. The time delay τ is introduced for the idler field via the diagonal unitary transformation $\hat{b}_n \to \hat{b}_n e^{i\omega_n\tau}$. The transformation for 50:50 beamsplitter is given by $\hat{c}_n = \frac{1}{\sqrt{2}}(\hat{a}_n + \hat{b}_n)$, $\hat{d}_n = \frac{1}{\sqrt{2}}(\hat{a}_n - \hat{b}_n)$, where $\hat{c}_n$ and $\hat{d}_n$ are the output annihilation operators [see Fig. 1(b)]. In matrix form, such input-output relation reads

$$\begin{pmatrix}\hat{\mathbf{c}}\\ \hat{\mathbf{d}}\end{pmatrix} = \mathcal{U}(\tau)\begin{pmatrix}\hat{\mathbf{a}}\\ \hat{\mathbf{b}}\end{pmatrix}, \tag{18}$$

where

$$\mathcal{U}(\tau) = \frac{1}{\sqrt{2}}\begin{pmatrix}\mathbf{1}_N & \mathbf{1}_N\\ \mathbf{1}_N & -\mathbf{1}_N\end{pmatrix}\begin{pmatrix}\mathbf{1}_N & 0\\ 0 & V(\tau)\end{pmatrix}, \tag{19}$$

$\mathbf{1}_N$ is the identity matrix and $V(\tau) = \mathrm{diag}(e^{i\omega_1\tau}, \ldots, e^{i\omega_N\tau})$ is the diagonal matrix.

Having the unitary transformation $\mathcal{U}(\tau)$ for operators, the second-order correlation matrices $\mathcal{D}$ and $\mathcal{C}$ are transformed as [18]

$$\mathcal{F} = \mathcal{U}^*(\tau)\,\mathcal{D}\,\mathcal{U}^T(\tau), \quad \mathcal{E} = \mathcal{U}(\tau)\,\mathcal{C}\,\mathcal{U}^T(\tau), \tag{20}$$

where resulting correlation matrices are

$$\mathcal{F}(z) = \begin{pmatrix}\langle\hat{\mathbf{c}}^\dagger\hat{\mathbf{c}}\rangle_z & \langle\hat{\mathbf{c}}^\dagger\hat{\mathbf{d}}\rangle_z\\ \langle\hat{\mathbf{d}}^\dagger\hat{\mathbf{c}}\rangle_z & \langle\hat{\mathbf{d}}^\dagger\hat{\mathbf{d}}\rangle_z\end{pmatrix}, \quad \mathcal{E}(z) = \begin{pmatrix}\langle\hat{\mathbf{c}}\hat{\mathbf{c}}\rangle_z & \langle\hat{\mathbf{c}}\hat{\mathbf{d}}\rangle_z\\ \langle\hat{\mathbf{d}}\hat{\mathbf{c}}\rangle_z & \langle\hat{\mathbf{d}}\hat{\mathbf{d}}\rangle_z\end{pmatrix}. \tag{21}$$

b. Photon-click detectors. For the HOM interferometer, we use two frequency-non-resolving photon-click detectors (on-off detectors), placed in both the signal and idler channels [Fig. 1(b)]. This type of detector does not distinguish the number of detected photons and their frequencies and is commonly used in HOM experiments [39].

Consider a state $\hat{\rho}$, which consists of two subsystems c and d. The detection operator for the subsystem i reads

$$\hat{\Pi}_i = \hat{I} - |\mathbf{0}\rangle\,\langle\mathbf{0}|_i\,, \tag{22}$$

where $i \in [c, d]$ and $|\mathbf{0}\rangle_i = \bigotimes_n |0\rangle_i$ is a vacuum state for the i-th subsystem and $\hat{I}$ is the identity operator. Then the probability of click detection in channel c is

$$P_c = \mathrm{Tr}(\hat{\Pi}_c \otimes \hat{I}_d\ \hat{\rho}) = 1 - q_c, \tag{23}$$

where

$$q_c = \mathrm{Tr}(|\mathbf{0}\rangle\,\langle\mathbf{0}|_c \otimes \hat{I}_d\ \hat{\rho}) = \langle\mathbf{0}|\hat{\rho}_c|\mathbf{0}\rangle_c \tag{24}$$

and the matrix $\hat{\rho}_c = \mathrm{Tr}_d(\hat{\rho})$ is the density matrix for subsystem c. The expression for the click-detection probability in channel d is similar to channel c.

The coincidence probability of photon-click detection in both channels reads

$$P_{cd} = \mathrm{Tr}(\hat{\Pi}_c \otimes \hat{\Pi}_d\hat{\rho}) = 1 + q_{cd} - q_c - q_d, \tag{25}$$

where

$$q_{cd} = \mathrm{Tr}(|\mathbf{0}\rangle\,\langle\mathbf{0}|_c \otimes |\mathbf{0}\rangle\,\langle\mathbf{0}|_d\ \hat{\rho}) = \langle\mathbf{0}|\,\hat{\rho}\,|\mathbf{0}\rangle \tag{26}$$

is a probability of simultaneous detection of vacuum in both channels; $|\mathbf{0}\rangle = |\mathbf{0}\rangle_c \otimes |\mathbf{0}\rangle_d$.

The Eqs. (24) and (26) are nothing more than the fidelity between the states $\hat{\rho}_c$ (and $\hat{\rho}$) with the vacuum states $|\mathbf{0}\rangle_c$ (and $|\mathbf{0}\rangle$). For multimode Gaussian states, these fidelities can be expressed in terms of the covariance matrix ($\hbar = 2$) [40,41]

$$q_c = F(\sigma_c), \quad q_{cd} = F(\sigma_{cd}). \tag{27}$$

where

$$F(\sigma) = \frac{2^M}{\sqrt{\det(\sigma + \mathbf{1}_{2M})}}, \tag{28}$$

$2M$ is the dimension of the covariance matrix σ, and $\mathbf{1}_{2M}$ is a $2M \times 2M$ identity matrix. In Appendix A, the equations for the covariance matrix are given explicitly. Similar results for probabilities can be obtained via the Torontonian function, which was used in Gaussian boson-sampling with threshold detectors [42].

E. Normalized second-order correlation function

The normalized second-order correlation function $g^{(2)}$ reveals additional temporal properties of the generated state. By definition [43], the normalized second-order correlation function reads

$$g^{(2)}(t_1,t_2,t_3,t_4)=\frac{\left\langle\prod_{i=1}^{2}\hat{E}^{(-)}(t_i)\prod_{j=3}^{4}\hat{E}^{(+)}(t_j)\right\rangle}{\prod_{i=1}^{4}\sqrt{G^{(1)}(t_i)}},\qquad(29)$$

where $G^{(1)}(t_i)=\langle\hat{E}^{(-)}(t_i)\hat{E}^{(+)}(t_i)\rangle$ is the first-order correlation function.

For pulsed multimode optical fields, the measurement of the normalized second-order correlation function in the form of Eq. (29) is quite challenging. Indeed, for short pulses, electric field fluctuations inside the pulse are present, which requires the use of nonlinear optical effects for a complete $g^{(2)}$ measurement, e.g., two-photon absorption or second harmonic generation [44,45], which is problematic for weak optical fields. Usually, such weak fields are measured via detectors, whose detection times are much larger than the pulse duration. Such detectors cannot resolve the fast field fluctuations, however, the averaged $g^{(2)}$ value is usually used for an estimation of the number of PDC spectral modes [13,46]. In this case, the averaged $g_s^{(2)}$ value and the number of modes μ_a for the signal field are related as

$$g_s^{(2)}=1+1/\mu_a.\qquad(30)$$

For $\mu_a\geqslant 1$, $g_s^{(2)}\leqslant 2$, while the equality holds for the spectrally single-mode regime. The $g_i^{(2)}$ for the idler field is calculated in a similar manner as for the signal field.

In experiments with low-gain PDC, the second-order correlation function is usually measured via a coincidence scheme with frequency-unresolved click detectors; the scheme is depicted in Fig. 1(c). Then, the measurement-based normalized second-order correlation function for the signal field is given by

$$\tilde{g}_s^{(2)}=\frac{P_{cd}^s}{P_c^s P_d^s},\qquad(31)$$

where P_{cd}^s is the coincidence probability and P_c^s and P_d^s are the detection probabilities in the channels "c" and "d," respectively. To compute probabilities P_{cd}^s, P_c^s and P_d^s for the signal field with Eqs. (23) and (25), we block the generated idler field [channel "b" in Fig. 1(c)] and insert a new vacuum field instead. Then, the state before the beamsplitter is given by the correlation matrices

$$\mathcal{D}(z)=\begin{pmatrix}\langle\hat{\mathbf{a}}^\dagger\hat{\mathbf{a}}\rangle_z & \mathbf{0}_N\\ \mathbf{0}_N & \mathbf{0}_N\end{pmatrix},\quad \mathcal{C}(z)=\begin{pmatrix}\langle\hat{\mathbf{a}}\hat{\mathbf{a}}\rangle_z & \mathbf{0}_N\\ \mathbf{0}_N & \mathbf{0}_N\end{pmatrix}.\qquad(32)$$

The state after the beamsplitter is given by the transformation Eq. (20) with $\mathcal{U}(\tau=0)$. From Eq. (23), the probabilities P_c^s and P_d^s are calculated and from Eq. (25) — the coincidence probability P_{cd}^s.

F. Summary

Before presenting the numerical results, we emphasize the advantages of our description. First, our approach is based on the framework of Gaussian states. The spatial Langevin and master equations obey causality (spatial ordering), i.e., the time-ordering effects are taken into account for the generated PDC field in the presence of internal losses. Particularly important is the validity of these equations for highly-dispersive media, where the high-order dispersion terms play a significant role. For example, the presence of group-velocity dispersion causes the spectral chirp, which is significant for the PDC generation with the use of ultrashort pulses. Second, the correlation matrices $\mathcal{D}$ and $\mathcal{C}$ contain all the information about the generated mixed state. This means that higher Fock-state contributions are taken into account, thereby moving beyond the usual spontaneous PDC (or low-gain PDC) approximation. The presented approach leads to the correct determination of the resulting $g^{(2)}$ values for the signal and idler fields in the presence of losses and at strong pumping.

The presented model eliminates the commonly used low-gain and lossless assumptions and is valid for spatially single-mode PDC and where higher-order nonlinear effects can be neglected. However, our model can be simply extended to the multimode waveguides and waveguide arrays: The presence of additional spatial modes increases the dimensionality, but the generated state remains to be Gaussian. Incorporating additional nonlinear optical processes is more challenging. For example, the cascaded up-conversion [47] is described by a Gaussian framework and therefore can be considered in terms of Gaussian master equations. However, the effects of pump-depletion [48,49] or self- and cross-phase modulation of the pump [50] produce non-Gaussian states, for which the solution in terms of the correlation matrices $\mathcal{D}$ and $\mathcal{C}$ is not sufficient.

III. NUMERICAL RESULTS AND DISCUSSION

To generate frequency-degenerate type-II PDC, we consider a $L=1$ cm-long waveguide with manually defined dispersion and losses. As a pump, we use a Gaussian pulse with a full width at half maximum of $\Delta\tau=0.5$ ps and a central wavelength of $\lambda_p=755$ nm.

So far as we consider long pulses with narrow spectra, we can limit ourselves to the first-order refractive index expansion for the pump, signal, and idler waves, i.e., we do not consider group-velocity dispersion or chirp in the waveguide. In this case, the refractive index for each field is taken to be

$$n(\omega)=n(\omega_0)+\frac{\omega-\omega_0}{\omega_0}\left[\frac{c}{v_g(\omega_0)}-n(\omega_0)\right],\qquad(33)$$

where c is the speed of light and v_g is the group velocity. In order to model a waveguide, we choose the following parameters: the pump refractive index $n_p=n(\omega_p)=1.9$ and group velocity $v_g^p=0.9c/n_p$, the signal refractive index $n_s=n(\omega_p/2)=1.9$ and group velocity $v_g^s=0.95v_g^p$, the idler refractive index $n_i=n(\omega_p/2)=1.8$ and group velocity $v_g^i=v_g^p$. Note that here we study the regime of group-velocity-matching between the pump and idler waves. Experimentally, such type of phase-matching was studied in, e.g., Ref. [16]. The quasi-phase-matching is obtained with $k_{\mathrm{QPM}}=\frac{\omega_p}{2c}(2n_p-n_s-n_i)$. The initial state and the state of the environment are taken to be vacuum. The pump is assumed to be nonscattered ($\alpha^p=0$). Below we study the case of spontaneous PDC with $\Gamma L\ll 1$ and $\langle\hat{n}\rangle\ll 1$. The numerical dataset is published in Ref. [51].

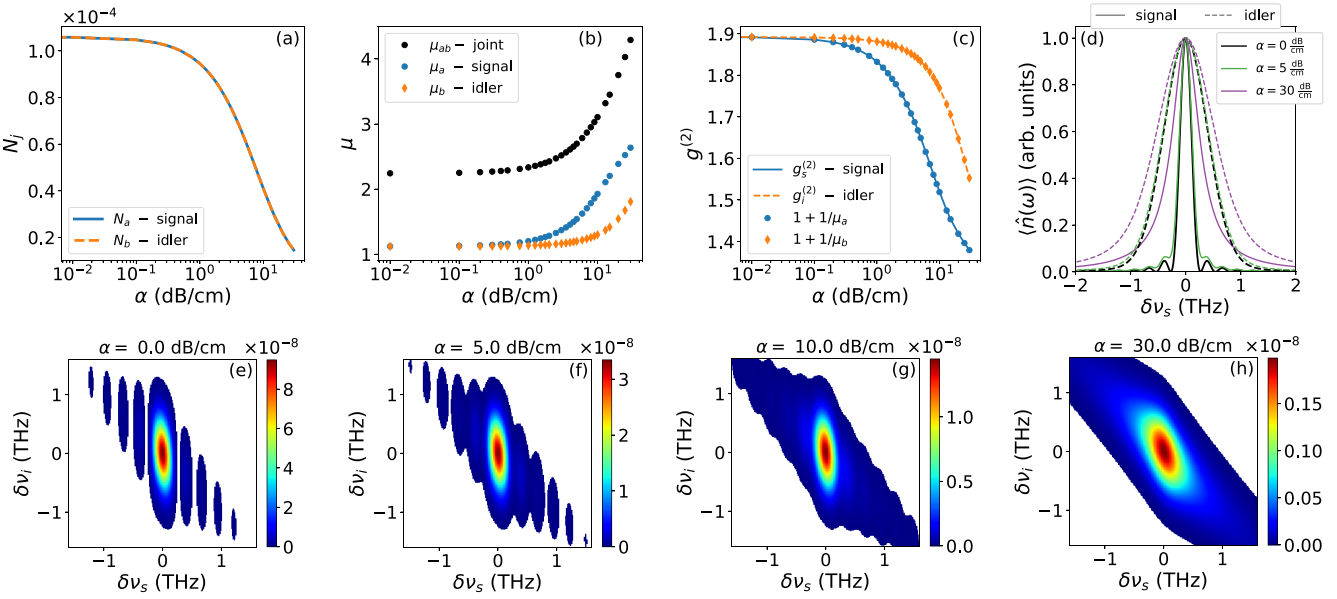

FIG. 2. (a) Total number of photons for the signal and idler fields as a function of the loss coefficient α; (b) number of occupied Mercer-Wolf modes μ_{ab}, μ_a and μ_b for the joint system, signal and idler subsystems, respectively; (c) the measurement-based second-order correlation function $g_j^{(2)}$ for the signal and idler fields as a function of α; (d) normalized signal and idler spectra for the lossless PDC $\alpha = 0$ dB/cm and lossy PDC with $\alpha = 5$ dB/cm and $\alpha = 30$ dB/cm; (e)–(h) JSI for the lossless PDC with $\alpha = 0$ dB/cm and lossy PDC with $\alpha = 5$ dB/cm, $\alpha = 10$ dB/cm and $\alpha = 30$ dB/cm, respectively. The white regions correspond to the values of the JSI below 0.4% of its maximal value. In (d)–(h), $\delta\nu$ is the detuning from the central frequency of PDC $\nu_p/2$.

As we will show below, the considered parameters provide the PDC generation with the spectral bandwidth of ≈5 nm around 1550 nm. The variation of the loss coefficient in such a small spectral range is usually small enough [8] to assume the losses to be frequency-independent.

A. Waveguide with equal losses

In the first subsection, we present the numerical results for a waveguide with frequency-independent and equal losses for the signal and idler fields $\alpha^a(\omega_n) = \alpha^b(\omega_n) \equiv \alpha$.

1. Spectral properties

In Fig. 2, the numerical results for the considered waveguide are presented. The number of photons for the signal and idler fields as a function of the loss parameter α is shown in Fig. 2(a). For lossless PDC, the average number of PDC photons per pulse reads $N = N_a + N_b = 2.1 \times 10^{-4}$, which corresponds to the spontaneous regime of PDC. As expected, the number of photons decreases with the increasing loss coefficient. So far as we consider equal losses for the signal and idler fields, the dependencies for the signal and idler fields coincide.

In contrast to the number of photons, the effective number of occupied PDC modes increases with the loss coefficient [see Fig. 2(b)]. For lossless PDC $\mu_{ab} = 2.2$, while its change for $\alpha < 0.5$ dB/cm is less than 2%. Starting from $\alpha \approx 1$ dB/cm, the number of modes increases significantly.

In addition, the dependencies of the effective number of occupied modes for the signal (μ_a) and idler (μ_b) subsystems are shown in Fig. 2(b) and illustrate the same tendency of increasing numbers of modes with the loss coefficient. However, despite considering equal losses in both channels, these dependencies are different, which indicates different spectral and temporal structures of the signal and idler subsystems. The modification of the mode structure of PDC is also illustrated in Fig. 2(c), where the $g_{s,i}^{(2)}$ and $\tilde{g}_{s,i}^{(2)}$ for the signal and idler fields are presented [Eqs. (31) and (30)]. These dependencies coincide $g_{s,i}^{(2)} = \tilde{g}_{s,i}^{(2)}$; therefore, the coincidence scheme with the click detectors can be used for the experimental determination of the number of modes μ_a and μ_b also for the mixed PDC state.

In order to study the influence of losses on the spectral properties of PDC, the spectra of signal and idler fields are shown in Fig. 2(d) for different amounts of losses: lossless PDC with $\alpha = 0$ dB/cm, $\alpha = 5$ dB/cm and $\alpha = 30$ dB/cm. Despite the noticeable amount of losses of $\alpha = 5$ dB/cm, the spectra do not differ significantly from the lossless PDC: only the visibility of oscillations in the signal spectrum decreases, while the spectral width remains almost the same.

For large losses, the difference in the spectrum becomes more prominent: The oscillations in the signal spectrum disappear and the spectrum broadens in comparison to the lossless case. Qualitatively, one can understand this as an effective reduction of the length of the nonlinear medium. This makes sense as high losses mean that photons, generated at the beginning of the waveguide, are most likely to be scattered. Therefore, photons exiting the system are significantly more likely to have been generated at the end of the medium. These effects are also revealed in the JSI. In Figs. 2(e)–2(h), the JSI for different losses is shown.

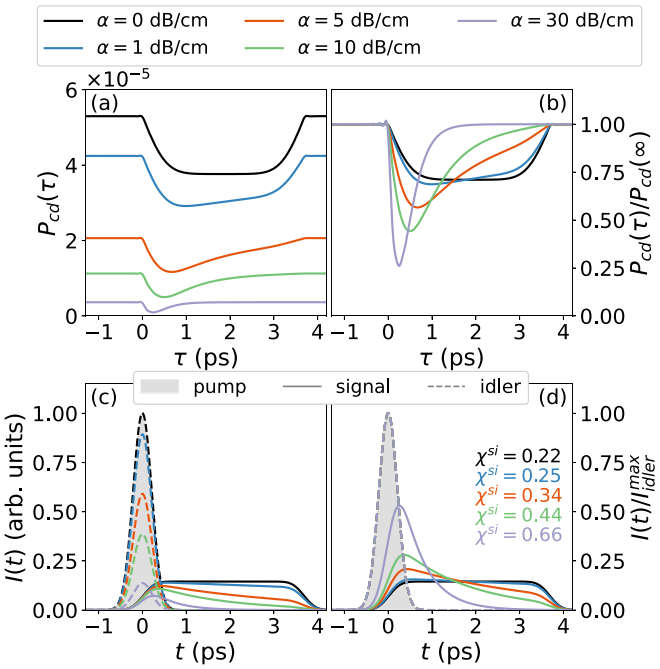

FIG. 3. (a), (b) The absolute and normalized HOM interference patterns; (c) temporal profiles of the signal and idler fields; (d) signal and idler temporal profiles normalized to the maximal value of the idler field. Different colors correspond to different values of α; different line-styles in (c), (d) correspond to signal and idler field. The filled area represents the temporal profile of the pump field. In (d), the temporal profiles of idler fields coincide. The overlap integrals for signal and idler temporal profiles $\chi^{si} = \frac{1}{C}\int dt I_s(t) I_i(t)$, where $C = \sqrt{\int dt I_s^2(t)}\sqrt{\int dt I_i^2(t)}$ are presented in (d) for different values of α by different color.

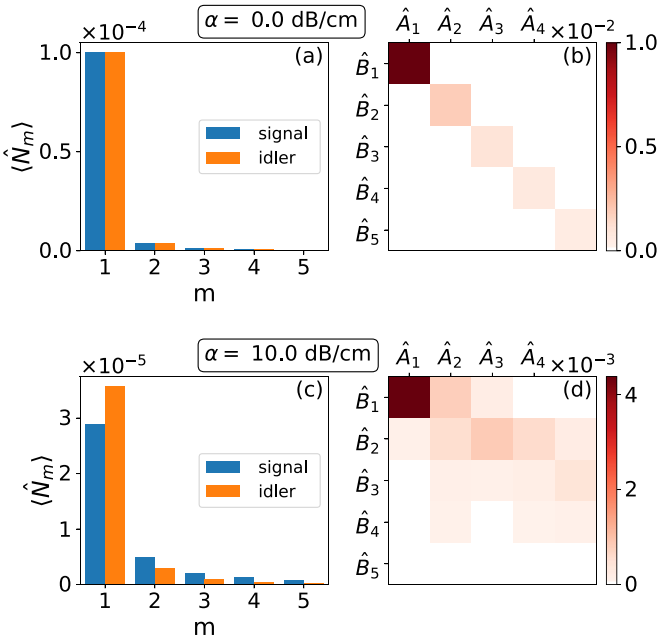

FIG. 4. The correlation matrices $\langle \hat{\mathbf{A}}^\dagger \hat{\mathbf{A}} \rangle$, $\langle \hat{\mathbf{B}}^\dagger \hat{\mathbf{B}} \rangle$ and $\langle \hat{\mathbf{A}} \hat{\mathbf{B}} \rangle$ in the Mercer-Wolf basis for the waveguides with (a), (b) $\alpha = 0$ dB/cm and (c), (d) $\alpha = 10$ dB/cm. In (a), (c) the distributions of the number of photons over the mode number are given for the signal $\langle \hat{N}_m \rangle = \langle \hat{A}_m^\dagger \hat{A}_m \rangle$ and idler $\langle \hat{N}_m \rangle = \langle \hat{B}_m^\dagger \hat{B}_m \rangle$ subsystems, respectively. Note that the off-diagonal elements for these matrices are absent in the Mercer-Wolf basis: $\langle \hat{A}_n^\dagger \hat{A}_m \rangle = \langle \hat{B}_n^\dagger \hat{B}_m \rangle = 0$, if $n \neq m$. In (b), (d), the absolute values of elements of the correlation matrix $\langle \hat{\mathbf{A}} \hat{\mathbf{B}} \rangle$ are shown.

2. Temporal properties

In Figs. 3(a) and 3(b), the HOM patterns are presented. First, in Fig. 3(a), the absolute values of coincidence probabilities between detectors are given for lossless PDC and lossy PDC. The increase in α leads to a decrease in the maximal coincidence probability. In addition, the shape of the interference pattern is changed, which is explicitly demonstrated for the normalized coincidence probabilities in Fig. 3(b). As the losses increase, one can notice that the visibility of the HOM interference increases while the temporal width of the HOM dip decreases.

To explain all observed effects, the temporal profiles of the signal and idler fields are shown in Figs. 3(c) and 3(d). Since the group velocity of the pump field equals the group velocity of the idler field, the temporal profiles of the pump and idler fields coincide. In turn, the signal field is slower. During the pump propagation along the waveguide, the generated signal photons are delayed with respect to the pump pulse, which results in a temporal profile of the signal field that has a large plateau. The earlier the signal photons are generated, the more delayed they are with respect to the pump. This effect is known as a temporal walk-off [5].

In the presence of losses, the photons are scattered, reducing the intensity of the PDC fields for both the signal and the idler fields. The idler pulse profile does not change significantly, while the signal pulse shape reveals a skew. This skew can be interpreted in the following manner: The amount of lost photons is proportional to the traveled distance inside the scattering medium. The photons generated at the beginning of the waveguide are more likely to be scattered, compared to the photons generated in the middle and in the end of the waveguide. Due to the temporal walk-off, we observe this effect as a skew in the temporal profile of the signal field. On the opposite, the idler temporal profile completely coincides with the pump, and its shape does not change with losses. Nevertheless, for $\alpha_s = \alpha_i$, it reveals the same amount of losses as the signal field, which can be noticed in Fig. 2(a), showing the total number of photons in each subsystem.

Despite such a destructive behavior of losses, they increase the overlap between the resulting signal and idler fields [see Fig. 3(d)]. The increased similarity between the temporal profiles of the signal and idler photons leads to an increasing visibility of the HOM dip. Higher visibility is usually interpreted as better biphoton indistinguishability, so high internal losses can reduce the difference in temporal profiles of signal and idler fields and make them more indistinguishable.

3. Mode structure

The dependence of the spectral and temporal profiles of PDC on the internal losses demonstrates that the mode structure of the generated light changes with losses. However, it may seem surprising that the case of equal internal losses leads to a different number of signal μ_a and idler μ_b modes [see Fig. 2(b)]. To explain this in more detail, we plot in Fig. 4 the correlation matrices $\langle \hat{\mathbf{A}}^\dagger \hat{\mathbf{A}} \rangle$, $\langle \hat{\mathbf{B}}^\dagger \hat{\mathbf{B}} \rangle$ and $\langle \hat{\mathbf{A}} \hat{\mathbf{B}} \rangle$ in the

Mercer-Wolf basis for both the lossless and lossy waveguides. Regardless of the waveguide losses, the matrices $\langle \hat{\mathbf{A}}^\dagger \hat{\mathbf{A}} \rangle$ and $\langle \hat{\mathbf{B}}^\dagger \hat{\mathbf{B}} \rangle$ are diagonal; their diagonal elements give the number of photons per mode for the signal and idler subsystems, respectively. For the lossless waveguide, the number of photons per mode for the signal and idler subsystems coincide [Fig. 4(a)]; therefore, $\mu_a = \mu_b$. In turn, the matrix $\langle \hat{\mathbf{A}}\hat{\mathbf{B}} \rangle$ is diagonal, i.e., the signal and idler modes are pairwise correlated [Fig. 4(b)], which means that we have perfectly correlated pairs of photons.

In the lossy waveguide, the behavior of correlation matrices differs compared to the lossless case. First, we note that the total number of photons in each channel is the same, while the photon number distribution over the modes is different [Fig. 4(c)]. This results in a different number of modes in the signal and idler beams; namely, $\mu_a \neq \mu_b$. Second, nondiagonal elements appear in the matrix $\langle \hat{\mathbf{A}}\hat{\mathbf{B}} \rangle$ [Fig. 4(d)]. These nondiagonal matrix elements $\langle \hat{A}_n \hat{B}_m \rangle$ with $n \neq m$ indicate the presence of cross-correlation between modes with different indices. From the point of view of photon correlations, it means that the pairs of photons generated in the PDC process can belong to different modes.

There is a physical interpretation of how these cross-correlations appear: In the presence of internal losses, the PDC photons are generated not only from the initial vacuum fluctuations (at the input of the waveguide), but also from the additional vacuum noise that enters the waveguide. At each coordinate z', this uncorrelated vacuum noise from the environment can contribute to different broadband modes. This contribution causes the presence of cross-correlations between different broadband modes in the PDC process generated at $z > z'$.

For the studied case, the phase-matching condition is not symmetrical with respect to the signal and idler subsystems: the signal field is slower compared to the pump and idler waves. In the presence of internal losses, this asymmetry between the signal and idler fields provides an asymmetric interaction with the environment, which is noticeable e.g. in the temporal profiles in Fig. 3. In other words, the asymmetric phase-matching conditions define how the vacuum modes of the environment contribute to the generated broadband modes, leading to asymmetry in the matrix $\langle \hat{\mathbf{A}}\hat{\mathbf{B}} \rangle$. During the PDC generation, at each coordinate z', the matrix $\langle \hat{\mathbf{a}}\hat{\mathbf{b}} \rangle$ —in other words the asymmetric matrix $\langle \hat{\mathbf{A}}\hat{\mathbf{B}} \rangle$— is coupled with the matrices $\langle \hat{\mathbf{a}}^\dagger \hat{\mathbf{a}} \rangle$ and $\langle \hat{\mathbf{b}}^\dagger \hat{\mathbf{b}} \rangle$ according to Eqs. (6) and (7). For the PDC generated at $z > z'$, this coupling causes a different photon-number distribution for the signal and idler beams, see Fig. 4(c) that provides a different number of modes $\mu_a \neq \mu_b$ and, consequently, different values of the second-order correlation function $g_s^{(2)} \neq g_i^{(2)}$.

Note that we study the PDC under the pump-idler group-velocity-matching condition. Different types of phase-matching conditions (e.g., symmetric group-velocity-matching) need additional studies, and we leave these cases out of the scope of this paper.

B. Waveguide with non-equal losses

Usually, the TE- and TM-modes of a waveguide reveal different scattering losses [7,8], therefore in this section, we present numerical results for the type-II PDC generated in a lossy waveguide with non-equal losses for the signal and idler fields.

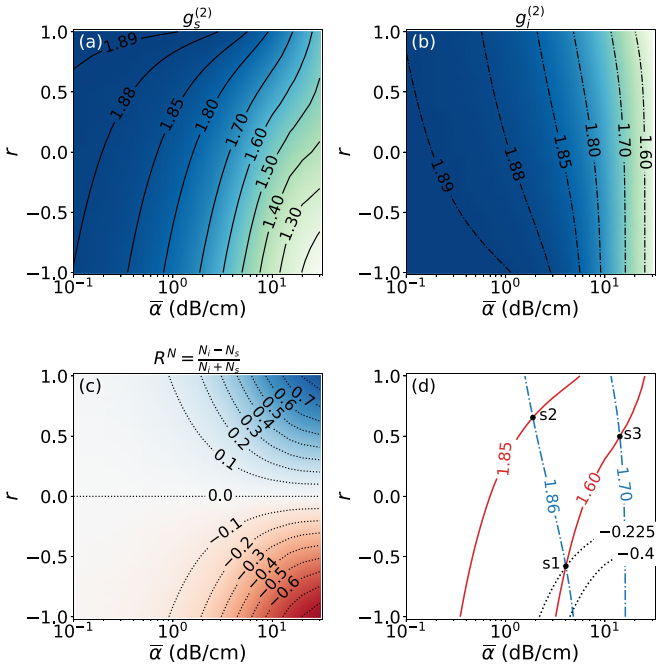

FIG. 5. (a)–(c) The dependencies of $g_s^{(2)}$, $g_i^{(2)}$ and R^N on $\bar{\alpha}$ and r, respectively. The waveguide dispersion and the pump profile are the same as in Sec. III. (d) The black dots indicate the intersection of two isolines, $g_s^{(2)}$ (red, solid) and $g_i^{(2)}$ (blue, dash-dotted), that correspond to the "measured" $g^{(2)}$ values. The black dotted curves depict the isolines of R^N. (point s1) $g_s^{(2)} = 1.6$ and $g_i^{(2)} = 1.86$, which gives the estimated values $\bar{\alpha}_1 = 4.0$ dB/cm and $r_1 = -0.57$, (point s2) $g_s^{(2)} = 1.85$ and $g_i^{(2)} = 1.86$, which gives the estimated values $\bar{\alpha}_2 = 1.9$ dB/cm and $r_2 = 0.65$, (point s3) $g_s^{(2)} = 1.6$ and $g_i^{(2)} = 1.7$, which gives the estimated values $\bar{\alpha}_3 = 14$ dB/cm and $r_3 = 0.49$.

As in the previous section, we consider the case of frequency-independent losses for both the signal (TE-mode) $\alpha^a(\omega_n) \equiv \alpha_s$ and idler (TM-mode) $\alpha^b(\omega_n) \equiv \alpha_i$ subsystems. In this case, we can parametrize the losses as

$$\bar{\alpha} = \frac{\alpha_s + \alpha_i}{2}, \quad r = \frac{\alpha_s - \alpha_i}{\alpha_s + \alpha_i}, \tag{34}$$

where $\bar{\alpha}$ can be interpreted as an average loss, and r is a loss ratio. The case $r \neq 0$ corresponds to the non-equal losses for the signal and idler subsystems.

For numerical simulations, we use the same waveguide dispersion and pump profile defined at the beginning of the Sec. III. The case of $r = 0$ and $\bar{\alpha} = \alpha$ corresponds to the waveguide studied in Sec. III A.

In Figs. 5(a)–5(c), the dependencies of $g_s^{(2)}$, $g_i^{(2)}$ and the relative number of photons

$$R^N = \frac{N_i - N_s}{N_s + N_i} \tag{35}$$

are presented as a function of the internal waveguide losses $\bar{\alpha}$ and r. A non-zero value of r leads to different numbers of photons in the signal and idler subsystems. In addition, the $g_s^{(2)}(\bar{\alpha}, r)$ and $g_i^{(2)}(\bar{\alpha}, r)$ depend on r, indicating an additional

redistribution of the number of photons over the modes in the case of non-equal losses.

C. Toward a loss determination scheme

The results of the previous subsection demonstrate that the values of $g^{(2)}$ for the signal and idler modes depend differently on the internal losses $\bar{\alpha}$ and r. Since external frequency-independent losses (transmission losses) do not change the value of the normalized second-order correlation function (see Appendix B), the difference in $g^{(2)}$ between the signal and idler fields can be used as an indicator of the internal waveguide losses. In this section, we discuss how the measured values of $g^{(2)}$ might be applied to experimentally determine the internal losses of a waveguide.

Let us assume a waveguide with the known dispersion and a general case of non-equal frequency-independent loss coefficients for the signal and idler beams $\alpha_s \neq \alpha_i$, which are unknown and should be determined in the experiment. Let us assume that the theoretical values of $g_s^{(2)}(\bar{\alpha}, r)$, $g_i^{(2)}(\bar{\alpha}, r)$ and the relative number of photons at the waveguide output are also known. If the behavior of the fixed isolines $g_s^{(2)}$, $g_i^{(2)}$, and R^N are different in the parameter space, their intersection allows us to estimate the values of $\bar{\alpha}$ and r. Summing up, for a known waveguide, the internal losses can be experimentally determined from the measured values of $g_s^{(2)}$, $g_i^{(2)}$ and R^N.

As an example, let us consider the waveguide from the previous section, for which the dependencies of $g_s^{(2)}$, $g_i^{(2)}$, and R^N are shown in Figs. 5(a)–5(c). Let us consider that we have "measured" in an experiment some values of $g_s^{(2)}$ and $g_i^{(2)}$. In Fig. 5(d), we present three examples "s1," "s2," mand "s3." For each fixed "measured" values of $g_s^{(2)}$ and $g_i^{(2)}$, there are two theoretically calculated isolines (red, solid) and (blue, dash-dotted), respectively. Such isolines have an intersection point (black circles) that defines the amount of internal losses.

In Fig. 5(d), we also present two isolines for a relative number of photons R^N (black, dotted). The value R^N can verify that the theoretical model is consistent with measurements. For our example "s1," if the external losses are correctly accounted and the "measured" values of correlation functions read $g_s^{(2)} = 1.6$ and $g_i^{(2)} = 1.86$, one should experimentally obtain $R^N = -0.225$. If for the given values of $g_s^{(2)}$ and $g_i^{(2)}$ and correctly accounted external losses we measure another value of R^N (for example $R^N = -0.4$), then this indicates that our prior knowledge about the waveguide dispersion is not correct.

The obtained results can be used as a starting point for developing an experimental method to determine internal losses. The main advantage of the proposed scheme is that the second-order correlation function is insensitive to the frequency-independent external losses (transmission and detection) and therefore the values of $g_s^{(2)}$ and $g_i^{(2)}$ can be measured with high accuracy. However, obtaining theoretical values of $g_s^{(2)}$ and $g_i^{(2)}$ requires knowledge of the waveguide dispersion, and, consequently, the numerical solution of the master equations. For each SPDC configuration with the fixed phase-matching condition, the dependence of $g_s^{(2)}$ and $g_i^{(2)}$ on the parameters $\bar{\alpha}$ and r should be investigated individually and more thoroughly. In addition, the presence of higher spatial modes, frequency-dependent losses, or additional waveguide imperfections can significantly change the properties of the generated SPDC field and $g^{(2)}$ behavior. At the same time, the development of an accurate experimental method is quite challenging: issues such as sensitivity analysis, validity, and impact of the waveguide model simplifications must be taken into account. In our work, we have shown the basic principle of this method and leave more in-depth research as a follow-up work.

IV. CONCLUSIONS

In this work, we examine theoretically the spectral and temporal properties of low-gain broadband PDC generated in a lossy waveguide. Our theoretical approach is based on the formalism of Gaussian states and the Langevin equation and is adjusted for the weak parametric down-conversion process and photon-number unresolved detection.

Using the example of frequency-degenerate type-II PDC generated under the pump-idler group-velocity-matching condition, we show how internal losses of nonlinear waveguides change the properties of the generated light. We demonstrate that the influence of internal losses on the spectral profiles of the generated field is weak. However, the Hong-Ou-Mandel interference strongly depends on losses: the Hong-Ou-Mandel dip may increase with losses, while the correlation time decreases, which is explained in terms of the temporal profiles of the signal and idler fields.

One of the most important results is the dissimilar dependence of the number of modes of the signal and idler field on the internal losses (even when losses are equal). Such behavior becomes apparent in the second-order correlation functions of the signal and idler fields, which can be easily detected in experiments: Different values of second-order correlation functions indicate the presence of internal waveguide losses. Based on this effect, we show that the second-order correlation functions can, in principle, be used for the determination of internal losses in nonlinear waveguides. We believe that the results obtained in our work can be directly applied to experiments and will strongly improve the characterization of nonlinear waveguides.

ACKNOWLEDGMENTS

This work is supported by the "Photonic Quantum Computing" (PhoQC) project, funded by the Ministry for Culture and Science of the State of North-Rhine Westphalia (Grant No. PROFILNRW-2020-067). We acknowledge financial support of the Deutsche Forschungsgemeinschaft (DFG) via the Collaborative Research Center "Tailored Nonlinear Photonics" TRR 142/3 (Project No. 231447078, Subproject No. C10). We acknowledge support for the publication cost by the Open Access Publication Fund of Paderborn University.

DATA AVAILABILITY

The data that support the findings of this article are openly available [51].

APPENDIX A: COVARIANCE MATRIX

A covariance matrix is a real positive-definite symmetric matrix of the second-order moments of quadrature operators

[19]. In this paper, we define the quadrature operators ($\hbar = 2$) as $\hat{q}_i = \hat{c}_i^\dagger + \hat{c}_i$ and $\hat{p}_i = i(\hat{c}_i^\dagger - \hat{c}_i)$ with the commutation relations $[\hat{q}_n, \hat{p}_m] = 2i\delta_{nm}$.

For non-displaced quantum states with $\langle \hat{c}_i \rangle = 0$ and $\langle \hat{x}_i \rangle = 0$, the elements of the covariance matrix σ are given by

$$\sigma_{ij} = \frac{\langle \hat{x}_i \hat{x}_j + \hat{x}_j \hat{x}_i \rangle}{2}, \tag{A1}$$

where $\hat{x}_i$ are the elements of the vector $\hat{\mathbf{x}} = (\hat{q}_1, \hat{q}_2, \ldots, \hat{q}_{2N}, \hat{p}_1, \hat{p}_2, \ldots, \hat{p}_{2N})^T$. Having the second-order correlators $\langle \hat{c}_i^\dagger \hat{c}_j \rangle$ and $\langle \hat{c}_i \hat{c}_j \rangle$, the elements of the matrix σ are given by

$$\langle \hat{q}_i \hat{q}_j \rangle = \delta_{ij} + 2(\mathrm{Re}[\langle \hat{c}_i^\dagger \hat{c}_j \rangle] + \mathrm{Re}[\langle \hat{c}_i \hat{c}_j \rangle]), \tag{A2}$$

$$\langle \hat{p}_i \hat{p}_j \rangle = \delta_{ij} + 2(\mathrm{Re}[\langle \hat{c}_i^\dagger \hat{c}_j \rangle] - \mathrm{Re}[\langle \hat{c}_i \hat{c}_j \rangle]), \tag{A3}$$

$$\frac{\langle \hat{p}_i \hat{q}_j + \hat{q}_j \hat{p}_i \rangle}{2} = 2(\mathrm{Im}[\langle \hat{c}_i \hat{c}_j \rangle] - \mathrm{Im}[\langle \hat{c}_i^\dagger \hat{c}_j \rangle]). \tag{A4}$$

To build the covariance matrix of the joint signal-idler system σ^{ab}, the $\langle \hat{\mathbf{c}}^\dagger \hat{\mathbf{c}} \rangle = \mathcal{D}$ and $\langle \hat{\mathbf{c}} \hat{\mathbf{c}} \rangle = \mathcal{C}$ from the main text. In turn, a covariance matrix σ^a for the signal subsystem is defined by the matrices $\langle \hat{\mathbf{c}}^\dagger \hat{\mathbf{c}} \rangle = \langle \hat{\mathbf{a}}^\dagger \hat{\mathbf{a}} \rangle$ and $\langle \hat{\mathbf{c}} \hat{\mathbf{c}} \rangle = \langle \hat{\mathbf{a}} \hat{\mathbf{a}} \rangle$.

APPENDIX B: SECOND-ORDER CORRELATION FUNCTION AND EXTERNAL LOSSES

The normalized second-order correlation function is insensitive to external frequency-independent losses. Indeed, for the field $\hat{E}^{(+)}(t)$, the losses can be introduced via a virtual beamsplitter with transmission coefficient T. If the losses are the same for all frequencies, the field transformation has the form $\hat{E}^{(+)}(t) \to \sqrt{T}\hat{E}^{(+)}(t)$. By substitution of the transformed field into Eq. (29), the factors $\sqrt{T}$ cancel out, what keeps the function $g^{(2)}(t_1, t_2, t_3, t_4)$ unchanged.

As a result, the values $g_s^{(2)}$ and $g_i^{(2)}$ remain unchanged in the presence of frequency-independent external losses (transmission and detection losses). As long as for lossless PDC $g_s^{(2)} = g_i^{(2)}$, a difference $g_s^{(2)} - g_i^{(2)}$ can indicate the presence of internal losses during the PDC process.

[1] E. Pelucchi, G. Fagas, I. Aharonovich, D. Englund, E. Figueroa, Q. Gong, H. Hannes, J. Liu, C.-Y. Lu, N. Matsuda, J.-W. Pan, F. Schreck, F. Sciarrino, C. Silberhorn, J. Wang, and K. D. Jöns, The potential and global outlook of integrated photonics for quantum technologies, Nat. Rev. Phys. **4**, 194 (2022).

[2] M. N. Satyanarayan, A. Deepthy, and H. L. Bhat, Potassium titanyl phosphate and its isomorphs: Growth, properties, and applications, Crit. Rev. Solid State Mater. Sci. **24**, 103 (1999).

[3] G. Poberaj, H. Hu, W. Sohler, and P. Günter, Lithium niobate on insulator (LNOI) for micro-photonic devices, Laser Photon. Rev. **6**, 488 (2012).

[4] E. J. Stanton, J. Chiles, N. Nader, G. Moody, N. Volet, L. Chang, J. E. Bowers, S. Woo Nam, and R. P. Mirin, Efficient second harmonic generation in nanophotonic GaAs-on-insulator waveguides, Opt. Express **28**, 9521 (2020).

[5] G. P. Agrawal, *Nonlinear Fiber Optics*, 5th ed. (Elsevier, Academic Press, Oxford, UK, 2013).

[6] J. Mishra, M. Jankowski, A. Y. Hwang, H. S. Stokowski, T. P. McKenna, C. Langrock, E. Ng, D. Heydari, H. Mabuchi, A. H. Safavi-Naeini, and M. M. Fejer, Ultra-broadband mid-infrared generation in dispersion-engineered thin-film lithium niobate, Opt. Express **30**, 32752 (2022).

[7] D. Melati, A. Melloni, and F. Morichetti, Real photonic waveguides: Guiding light through imperfections, Adv. Opt. Photon. **6**, 156 (2014).

[8] M. Hammer, S. Babel, H. Farheen, L. Padberg, J. C. Scheytt, C. Silberhorn, and J. Förstner, Estimation of losses caused by sidewall roughness in thin-film lithium niobate rib and strip waveguides, Opt. Express **32**, 22878 (2024).

[9] M. Placke, J. Schlegel, F. Mann, P. Della Casa, A. Thies, M. Weyers, G. Tränkle, and S. Ramelow, Telecom-band spontaneous parametric down-conversion in AlGaAs-on-insulator waveguides, Laser Photon. Rev. **18**, 2301293 (2024).

[10] J. Schuhmann, L. Lazzari, M. Morassi, A. Lemaître, I. Sagnes, G. Beaudoin, M. Amanti, F. Boeuf, F. Raineri, F. Baboux, and S. Ducci, Hybrid III-V/silicon quantum photonic device generating broadband entangled photon pairs, PRX Quantum **5**, 040321 (2024).

[11] C. K. Hong, Z. Y. Ou, and L. Mandel, Measurement of subpicosecond time intervals between two photons by interference, Phys. Rev. Lett. **59**, 2044 (1987).

[12] M. Avenhaus, A. Eckstein, P. J. Mosley, and C. Silberhorn, Fiber-assisted single-photon spectrograph, Opt. Lett. **34**, 2873 (2009).

[13] A. Christ, K. Laiho, A. Eckstein, K. N. Cassemiro, and C. Silberhorn, Probing multimode squeezing with correlation functions, New J. Phys. **13**, 033027 (2011).

[14] K. Zielnicki, K. Garay-Palmett, D. Cruz-Delgado, H. Cruz-Ramirez, M. F. O'Boyle, B. Fang, V. O. Lorenz, A. B. U'Ren, and P. G. Kwiat, Joint spectral characterization of photon-pair sources, J. Mod. Opt. **65**, 1141 (2018).

[15] F. Graffitti, J. Kelly-Massicotte, A. Fedrizzi, and A. M. Brańczyk, Design considerations for high-purity heralded single-photon sources, Phys. Rev. A **98**, 053811 (2018).

[16] C. J. Xin, J. Mishra, C. Chen, D. Zhu, A. Shams-Ansari, C. Langrock, N. Sinclair, F. N. C. Wong, M. M. Fejer, and M. Lončar, Spectrally separable photon-pair generation in dispersion engineered thin-film lithium niobate, Opt. Lett. **47**, 2830 (2022).

[17] N. A. Lange, T. Schapeler, J. P. Höpker, M. Protte, and T. J. Bartley, Degenerate photons from a cryogenic spontaneous parametric down-conversion source, Phys. Rev. A **108**, 023701 (2023).

[18] D. A. Kopylov, T. Meier, and P. R. Sharapova, Theory of multimode squeezed light generation in lossy media, Quantum **9**, 1621 (2025).

[19] C. Weedbrook, S. Pirandola, R. García-Patrón, N. J. Cerf, T. C. Ralph, J. H. Shapiro, and S. Lloyd, Gaussian quantum information, Rev. Mod. Phys. **84**, 621 (2012).

[20] B. Huttner, S. Serulnik, and Y. Ben-Aryeh, Quantum analysis of light propagation in a parametric amplifier, Phys. Rev. A **42**, 5594 (1990).

[21] D. B. Horoshko, Generator of spatial evolution of the electromagnetic field, Phys. Rev. A **105**, 013708 (2022).
[22] W. Vogel and D.-G. Welsch, *Quantum Optics* (Wiley-VCH, Berlin, 2006).
[23] A. Christ, B. Brecht, W. Mauerer, and C. Silberhorn, Theory of quantum frequency conversion and type-II parametric down-conversion in the high-gain regime, New J. Phys. **15**, 053038 (2013).
[24] P. R. Sharapova, G. Frascella, M. Riabinin, A. M. Pérez, O. V. Tikhonova, S. Lemieux, R. W. Boyd, G. Leuchs, and M. V. Chekhova, Properties of bright squeezed vacuum at increasing brightness, Phys. Rev. Res. **2**, 013371 (2020).
[25] D. S. Phillips, M. Walschaers, J. J. Renema, I. A. Walmsley, N. Treps, and J. Sperling, Benchmarking of Gaussian boson sampling using two-point correlators, Phys. Rev. A **99**, 023836 (2019).
[26] E. Wolf, New theory of partial coherence in the space–frequency domain. Part I: Spectra and cross spectra of steady-state sources, J. Opt. Soc. Am. **72**, 343 (1982).
[27] L. Mandel and E. Wolf, *Optical Coherence and Quantum Optics* (Cambridge University Press, Cambridge, UK, 1995).
[28] C. Fabre and N. Treps, Modes and states in quantum optics, Rev. Mod. Phys. **92**, 035005 (2020).
[29] A. Eckstein, A. Christ, P. J. Mosley, and C. Silberhorn, Highly efficient single-pass source of pulsed single-mode twin beams of light, Phys. Rev. Lett. **106**, 013603 (2011).
[30] I. V. Dyakonov, P. R. Sharapova, T. S. Iskhakov, and G. Leuchs, Direct Schmidt number measurement of high-gain parametric down conversion, Laser Phys. Lett. **12**, 065202 (2015).
[31] W. P. Grice and I. A. Walmsley, Spectral information and distinguishability in type-II down-conversion with a broadband pump, Phys. Rev. A **56**, 1627 (1997).
[32] C. Drago and A. M. Braczyk, Hong–Ou–Mandel interference: A spectral–temporal analysis, Canadian J. Phys. **102**, 411 (2024).
[33] D. A. Antonosyan, A. S. Solntsev, and A. A. Sukhorukov, Effect of loss on photon-pair generation in nonlinear waveguide arrays, Phys. Rev. A **90**, 043845 (2014).
[34] D. N. Vavulin and A. A. Sukhorukov, Effect of loss on single photon parametric amplification, Opt. Commun. **390**, 117 (2017).
[35] M. Gräfe, D. A. Antonosyan, A. S. Solntsev, A. A. Sukhorukov, and A. Szameit, Optical emulation of photon-pair generation in nonlinear lossy waveguides, Europhys. Lett. **118**, 54001 (2017).
[36] L. G. Helt, M. J. Steel, and J. E. Sipe, Spontaneous parametric downconversion in waveguides: What's loss got to do with it? New J. Phys. **17**, 013055 (2015).
[37] A. N. Poddubny, I. V. Iorsh, and A. A. Sukhorukov, Generation of photon-plasmon quantum states in nonlinear hyperbolic metamaterials, Phys. Rev. Lett. **117**, 123901 (2016).
[38] M. Banic, L. Zatti, M. Liscidini, and J. E. Sipe, Two strategies for modeling nonlinear optics in lossy integrated photonic structures, Phys. Rev. A **106**, 043707 (2022).
[39] S. Babel, L. Bollmers, M. Massaro, K. H. Luo, M. Stefszky, F. Pegoraro, P. Held, H. Herrmann, C. Eigner, B. Brecht, L. Padberg, and C. Silberhorn, Demonstration of Hong-Ou-Mandel interference in an LNOI directional coupler, Opt. Express **31**, 23140 (2023).
[40] G. Spedalieri, C. Weedbrook, and S. Pirandola, A limit formula for the quantum fidelity, J. Phys. A: Math. Theor. **46**, 025304 (2013).
[41] L. Banchi, S. L. Braunstein, and S. Pirandola, Quantum fidelity for arbitrary Gaussian states, Phys. Rev. Lett. **115**, 260501 (2015).
[42] N. Quesada, J. M. Arrazola, and N. Killoran, Gaussian boson sampling using threshold detectors, Phys. Rev. A **98**, 062322 (2018).
[43] R. J. Glauber, The quantum theory of optical coherence, Phys. Rev. **130**, 2529 (1963).
[44] F. Boitier, A. Godard, N. Dubreuil, P. Delaye, C. Fabre, and E. Rosencher, Two-photon-counting interferometry, Phys. Rev. A **87**, 013844 (2013).
[45] D. A. Kopylov, A. V. Rasputnyi, T. V. Murzina, and M. V. Chekhova, Spectral properties of second, third and fourth harmonics generation from broadband multimode bright squeezed vacuum, Laser Phys. Lett. **17**, 075401 (2020).
[46] T. S. Iskhakov, A. M. Pérez, K. Y. Spasibko, M. V. Chekhova, and G. Leuchs, Superbunched bright squeezed vacuum state, Opt. Lett. **37**, 1919 (2012).
[47] A. V. Rasputnyi and D. A. Kopylov, Quantum spatial dynamics of high-gain parametric down-conversion accompanied by cascaded up-conversion, Phys. Rev. A **104**, 013702 (2021).
[48] J. Flórez, J. S. Lundeen, and M. V. Chekhova, Pump depletion in parametric down-conversion with low pump energies, Opt. Lett. **45**, 4264 (2020).
[49] K. Chinni and N. Quesada, Beyond the parametric approximation: Pump depletion, entanglement, and squeezing in macroscopic down-conversion, Phys. Rev. A **110**, 013712 (2024).
[50] N. Quesada, L. G. Helt, M. Menotti, M. Liscidini, and J. E. Sipe, Beyond photon pairs—nonlinear quantum photonics in the high-gain regime: A tutorial, Adv. Opt. Photon. **14**, 291 (2022).
[51] D. Kopylov, M. Stefszky, T. Meier, C. Silberhorn, and P. Sharapova, Spectral and temporal properties of type-II parametric down-conversion: The impact of losses during state generation [Data set], Zenodo (2025), DOI: 10.5281/zenodo.14802394.